remote sensing

MDPI

Article

Assessment of C-Band Polarimetric Radar for the Detection of Diesel Fuel in Newly Formed Sea Ice

Leah Hicks [1], Mahdi Zabihi Mayvan [1], Elvis Asihene [1], Durell S. Desmond [1], Katarzyna Polcwiartek [1], Gary A. Stern [1] and Dustin Isleifson [1,2,*]

[1] Centre for Earth Observation Science, University of Manitoba, Winnipeg, MB R3T 2N2, Canada; hickls@umanitoba.ca (L.H.); zabihimm@myumanitoba.ca (M.Z.M.)
[2] Department of Electrical and Computer Engineering, University of Manitoba, Winnipeg, MB R3T 5V6, Canada
* Correspondence: dustin.isleifson@umanitoba.ca; Tel.: +1-204-474-6553

Abstract: There is a heightened risk of an oil spill occurring in the Arctic, as climate change driven sea ice loss permits an increase in Arctic marine transportation. The ability to detect an oil spill and monitor its progression is key to enacting an effective response. Microwave scatterometer systems may be used detect changes in sea ice thermodynamic and physical properties, so we examined the potential of C-band polarimetric radar for detecting diesel fuel beneath a thin sea ice layer. Sea ice physical properties, including thickness, temperature, and salinity, were measured before and after diesel addition beneath the ice. Time-series polarimetric C-band scatterometer measurements monitored the sea ice evolution and diesel migration to the sea ice surface. We characterized the temporal evolution of the diesel-contaminated seawater and sea ice by monitoring the normalized radar cross section (NRCS) and polarimetric parameters (conformity coefficient (μ), copolarization correlation coefficient (ρco)) at 20° and 25° incidence angles. We delineated three stages, with distinct NRCS and polarimetric results, which could be connected to the thermophysical state and the presence of diesel on the surface. Stage 1 described the initial formation of sea ice, while in Stage 2, we injected 20L of diesel beneath the sea ice. No immediate response was noted in the radar measurements. With the emergence of diesel on the sea ice surface, denoted by Stage 3, the NRCS dropped substantially. The largest response was for VV and HH polarizations at 20° incidence angle. Physical sampling indicated that diesel emerged to the surface of the sea ice and trended towards the tub edge and the polarimetric scatterometer was sensitive to these physical changes. This study contributes to a greater understanding of how C-band frequencies can be used to monitor oil products in the Arctic and act as a baseline for the interpretation of satellite data. Additionally, these findings will assist in the development of standards for oil and diesel fuel detection in the Canadian Arctic in association with the Canadian Standards Association Group.

Keywords: Arctic; sea ice; oil spill; radar; scatterometer; diesel; C-band; polarimetry

check for updates

Citation: Hicks, L.; Zabihi Mayvan, M.; Asihene, E.; Desmond, D.S.; Polcwiartek, K.; Stern, G.A.; Isleifson, D. Assessment of C-Band Polarimetric Radar for the Detection of Diesel Fuel in Newly Formed Sea Ice. *Remote Sens.* **2024**, *16*, 2002. https://doi.org/10.3390/rs16112002

Academic Editor: Xiao Cheng

Received: 21 March 2024
Revised: 6 May 2024
Accepted: 27 May 2024
Published: 2 June 2024

Copyright: © 2024 by the authors. Licensee MDPI, Basel, Switzerland. This article is an open access article distributed under the terms and conditions of the Creative Commons Attribution (CC BY) license (https://creativecommons.org/licenses/by/4.0/).

1. Introduction

There is clear scientific consensus that climate change is drastically affecting the Arctic environment. This has resulted in a transition from a thick persistent multi-year sea ice cover to thinner first-year sea ice (FYI) and open water [1,2]. The presence of thinner FYI has given rise to increased ship traffic along the North-West Passage, and Hudson Bay shipping corridors [3] which, in turn, increases the chances of an accidental oil spill [4,5]. A spill could include a variety of oil products, and diesel is a particularly important product to understand, due to its abundant use in shipping and fuel transfer. Characteristics of the Arctic such as extreme weather, remoteness, lack of infrastructure, and the presence of sea ice, make spill detection and response extremely difficult [6,7].

Remote sensing methods have been used to monitor marine oil spills, but there is limited knowledge of sensor capability to detect and identify diesel fuel within and under

sea ice [8,9]. There is agreement within the scientific community that active microwave radar sensors are well suited for operation in the Arctic environment, as they provide their own illumination and are able to obtain information on sea ice-coverage [10]. Satellite-based radar sensors provide broad spatial coverage, which is necessary for monitoring vast regions, such as the Arctic. In contrast, surface-based systems, such as scatterometers, can provide detailed time-series data collection but are limited by location [11,12]. The most commonly used bands for sea ice monitoring are L-band (e.g., 1.26 GHz) and C-band (e.g., 5.5 GHz) [13]. The typical output of a scatterometer radar system is the normalized radar cross section (NRCS). Beyond this, the utility of polarimetric parameters, derived from the covariance matrix, has shown potential for determining physical scattering mechanisms [14–16]. These parameters, such as the copolarization (ρco) and conformity (μ) coefficients, have been used to analyze sea ice scattering mechanisms [17].

Variation in NRCS values results from thermophysical properties of sea ice (e.g., temperature, salinity, and brine volume) [18–20]. Sea ice dielectrics are influenced by brine volume content, salinity, and temperature, which in turn affect microwave backscatter [21]. The copolarization correlation coefficient is a parameter that has proven useful for distinguishing newly formed sea ice from water, as well as inhomogeneities within sea ice. The values range from 0 to 1 [17]. The conformity coefficient, μ, has been used to discriminate between smooth and rough surfaces [22]. In previous oil spill experiments in open water, μ has been used to discriminate between areas with oil and open ocean [22].

New sea ice is highly saline with concentrations ranging from 15 ppt to 25 ppt in ice thicknesses less than 5 cm, as sea ice grows brine is expelled to the surface of the ice and seawater below [23]. Salinity and brine volume profiles in first-year sea ice follow a characteristic C-shape, with high concentrations at the surface and bottom of the ice profile. Notably, the dielectric properties of sea ice tend to increase with increasing temperature, which impedes microwave penetration into sea ice [21]. The limited microwave penetration results in backscatter values that are mainly a result of surface scattering. Microwave scattering may also be influenced by the presence of slush on the surface at warmer temperatures, which impede microwave penetration [21].

An oil spill may be introduced into the marine environment through a variety of mechanisms (e.g., spills from vessels, or seeps from undersea reservoirs). The presence of sea ice influences the location and movement of oil based on the area coverage. If there is less than 30% sea ice the oil behaves as if it is in open water, while, if it is above 70%, the oil will move with the movement of sea ice [8]. Within sea ice coverage, an oil spill beneath the ice has also been observed to travel vertically in the sea ice through brine channels, cracks, and air gaps, due to a difference of densities [24,25]. Key properties that influence its behavior in an ice-infiltrated environment are the density (composition) of oil and the temperature and salinity of the sea ice [9]. Diesel fuel is often used for shipping and is a source of fuel for many remote northern communities in Canada, making it a risk for spills [26]. Diesel fuel is composed of a general mixture of C10 through C19 hydrocarbons and is denser than gasoline and jet fuel [27]. Based on the intended use of the diesel fuel, there may be additives present, these can include oxidation inhibitors, rust preventatives, and de-icers, additives will change the chemical composition of the diesel fuel [27].

The density of oil products influences how they will interact with the seawater and ice, and when the oil density is less than that of seawater it will migrate upwards through the ice [28,29]. The upward migration of oil may follow a C-shaped migration pattern (akin to bulk salinity) or may simply exhibit an increasingly larger magnitude towards the ice surface [24], whereby the vertical movement of oil in sea ice is greater than the horizontal movement [30]. Oil typically travels upward in the sea ice through brine channels and cracks. If oil moves through a brine channel, the brine will either be displaced towards the surface or subsurface of the sea ice [31]. The temperature and age of the sea ice influence how many brine channels are present, and therefore how easily oil can move up through the sea ice [24]. Increases in temperature are positively correlated to increases in brine volume within sea ice. However, when oil is present, increases in temperature and brine

volume cause a decrease in the salinity of the ice as oil moves up through the ice [31]. The presence of oil significantly influences the temperature of sea ice due to the decreased albedo of the ice and the insulating properties of the oil [8,9]. Once oil has traveled through brine channels in the sea ice it will pool on the surface of the ice, further impacting the temperature and presence of brine channels.

The behavior of oil products within sea ice contributes to the detection abilities of microwave scatterometer systems. Changes in sea ice salinity strongly impact microwave backscatter results from scatterometer systems as salinity is a critical factor in determining how far microwaves can penetrate the sea ice [32]. Studies that focused on detecting oil underneath and within sea ice at C-band noted that the oil was only detectable underneath thin ice or once it moved up through the ice to the surface [25]. An observed decrease in the returned backscatter values was also noted by researchers, likely resulting from the displacement of brine to the subsurface and subsequent smoothing of the ice surface [24]. Past studies have used C-band scatterometers to detect crude oil under FYI [24,25] but a better understanding of the usability of C-band scatterometers for the detection of diesel fuel underneath and within young sea ice is needed. Diesel fuel is one of the main fuel types used by ships and is the main source of energy for many remote northern communities in Canada. Additionally, the development of standards for early detection, monitoring, and identification of diesel fuel spills is vital in ensuring that proper mitigation procedures conducted by governments, industry, and local communities are implemented as soon as possible and that the Arctic environment is protected from severe damage.

The remoteness of the Arctic environment significantly limits the ability of early detection and response to oil spills [6]. Satellites, such as RADARSAT 2, prove to be a viable option for the early detection of oil and diesel spills in the Arctic, but there is a need to be able to validate the data received from these sensors. Previous work on detecting oil spills in sea ice environments have included studies ranging from airborne to satellite, multifrequency systems, and delineating oil spills from newly-formed sea ice or open water conditions [33–36].

The goal of this study is to build on the understanding of how a polarimetric C-band scatterometer system responds to the introduction of diesel fuel underneath newly formed sea ice. Specific objectives are to (1) measure and evaluate the time-series C-band scattering signatures during a freeze-up event, (2) to assess how C-band responds to changes in the thermodynamic properties of newly formed sea ice, and (3) to analyze how the polarimetric C-band results can be used to detect changes in response to the introduction of diesel fuel. The outcomes of this study will contribute to a greater understanding of how C-band frequencies can be used to monitor oil products in the Arctic, act as a baseline for the interpretation of satellite data and assist in the development of standards for oil and diesel fuel detection in the Canadian Arctic.

2. Methods

2.1. Description of Facility and Study Site Location

This study was conducted at the University of Manitoba Sea-ice Environmental Research Facility (SERF) from 6–9 March 2023 (see the next section for details on the timeline). SERF is an experimental research facility that is equipped with an outdoor clean seawater pool, as well as sea ice tubs that can be contaminated (Figure 1). The tubs can be heated with a removable heater for open seawater experiments and studies that focus on the growth of sea ice. This study was conducted in a tub that is 4 m in diameter and 1 m in depth and constructed with fiberglass. The seawater that is in the SERF tub is artificial, made from a chemical formulation of groundwater and salts [9,25]. For this study, the salinity of the water was 20.9 PSU which is notably lower than the Arctic Ocean, but similar to what can be found in an estuary [37]. SERF also has a local weather station that monitors the air temperature and relative humidity (Figure 1).

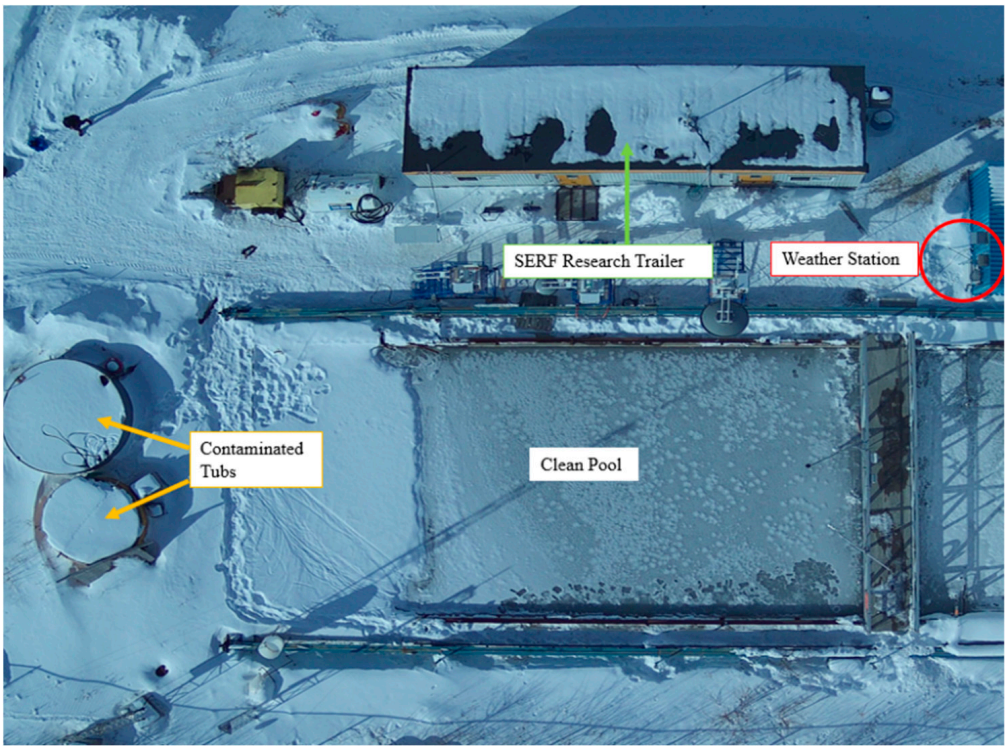


Figure 1. SERF Site Overview Prior to Experimental Setup.

Safety measures were put in place to ensure that proper protocols were followed. An orange fence was installed around the contaminated study area (Figure 2), which ensured that personnel without personal protective equipment (PPE) did not enter the area. Everyone who was involved in the collection of physical samples was required to wear personal protective equipment consisting of Tyvek suits, boots, gloves, and full-face respirators.

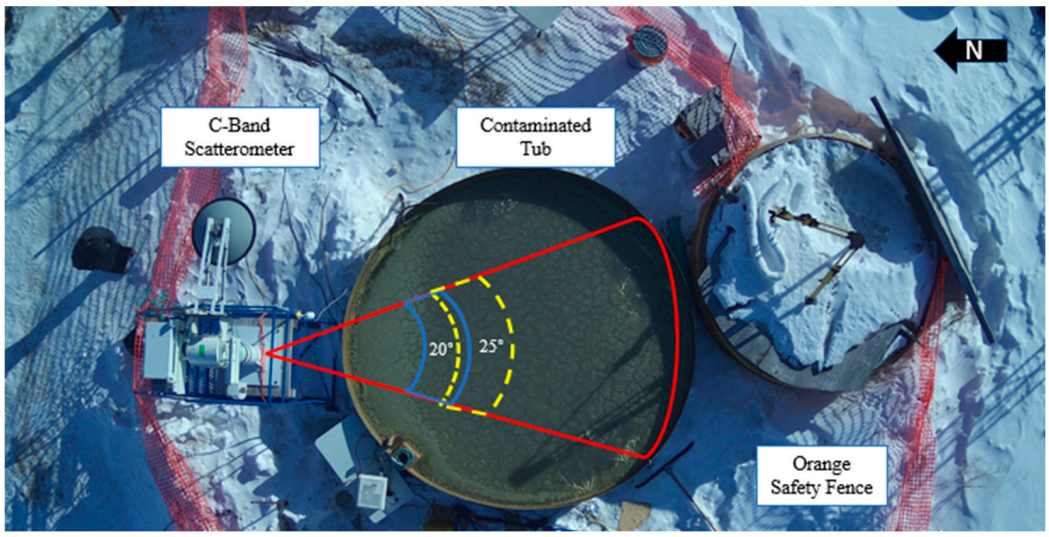


Figure 2. Experimental Setup at SERF and Radar Footprint of C-Scat (outlined in red). The highlighted areas represent the swaths of incidence angles used in this study after a careful inspection was done to eliminate errors associated with the edge of the tub. The solid blue line represents the incidence angle of 20° while the dashed yellow line is 25°.

2.2. Timeline of Study

This study was conducted from 6–9 March 2023. Scatterometer measurements started at 08:23 CST on 6 March 2023, and the heater was turned off at 08:30 CST on 6 March, which marks hour 0 of the experiment. Ice was allowed to naturally grow from 08:30 March 6 to 11:00 7 March, before diesel fuel was injected underneath the ice. A total of 20 L of diesel fuel was pumped into the water underneath sea ice over an hour. Following the injection, the conditions and physical properties of the sea ice and water were monitored until the end of the study at 09:00 on 9 March. Three distinct phases of the experiment were established based on ice formation and scatterometer results, Stage 1—open water (from 08:23 to 21:30 on 6 March), Stage 2—thin ice (21:30 6 March to 13:30 8 March), and Stage 3—diesel on ice (13:30 8 March–09:00 9 March).

2.3. Scatterometer Measurements

The C-band scatterometer (C-SCAT) used in this project was manufactured by ProSensing Inc. and has been used in previous oil spill and sea ice monitoring experiments [25,38,39]. The system has a positioner, an RF unit, and an antenna, which are controlled by a laptop computer with custom software. The positioner is a precision mechanical gearbox that can be commanded to point the antenna toward a target of interest. Within the RF unit, the scatterometer system uses a Frequency Modulated Continuous Wave (FMCW) architecture and operates at a center frequency of 5.5 GHz with a 500 MHz bandwidth. The antenna is a parabolic reflector dish with a pencil beam radiation pattern and high cross-polarization isolation. A summary of relevant system details can be found in Table 1. The system transmits and receives in four polarizations: horizontal–horizontal (HH), vertical–vertical (VV), horizontal–vertical (HV), and vertical–horizontal (VH), where the first index is the transmitted polarization and the second is the received polarization. For a user-defined scan configuration, with a specific azimuth swath and discrete elevation angles, C-SCAT operates with the positioner rotating about its axes and simultaneously sending and receiving pulses. For each elevation angle, an azimuth swath is performed while measuring the backscattered fields. It uses a covariance averaging process (see Equation (1)) to produce one value for each elevation. From this, the Normalized Radar Cross Section (NRCS), which considers the range to the target, system parameters, and area of illumination, is calculated.

Table 1. C-Band Scatterometer System Operating Specifications.

Center Frequency	5.5 GHz
Polarization Modes	HH, VV, HV, VH
Sweep Bandwidth	500 MHz
Transmitted Power	−6 dBm
Range Resolution	30 cm
Antenna Half Power	5.7°
Cross Polarization Isolation	>28 dB

The scatterometer system operating at C-band (C-SCAT) was installed at SERF on scaffolding adjacent to the contaminated tub at a height of 2.95 m (Figure 2). C-SCAT was configured to scan the tub four times every hour. The azimuth swath width was set to 30° and scans at 5° increments between 0° and 60° elevation angles were collected. C-SCAT is sensitive to scattering from the edges of the tub, so methods established by [38,39] were used to determine the angles that were not affected by the edges of the pool and surrounding objects. As a result, we are presenting only those elevation angles that were confirmed to be unaffected during our data processing.

2.4. Data Processing

Scatterometer NRCS data were processed in Interface Description Language (IDL) and analyzed in MATLAB. The footprint of the beam of C-SCAT was calculated for each elevation angle to determine which elevations would not be impacted by the edge of the pool. We determined that 20° and 25° angles were not impacted and thus will be the two elevation angles used for the rest of this study. We obtained the NRCS for VV, HH, and VH for these angles and a moving average filter (n = 4) was applied to present the time-series trend of the radar data. Copolarization correlation (ρco) and conformity (μ) coefficients were also calculated and plotted for the study period using Equations (2) and (3). These parameters have shown utility in monitoring freeze-up events, as well as detecting crude oil within sea ice [17].

$$\langle [\boldsymbol{C_3}] \rangle = \begin{bmatrix} \left\langle |S_{vv}|^2 \right\rangle & \sqrt{2}\left\langle S_{vv}{S_{vh}}^* \right\rangle & \left\langle S_{vv}{S_{hh}}^* \right\rangle \\ \sqrt{2}\left\langle S_{vh}{S_{vv}}^* \right\rangle & 2\left\langle |S_{vh}|^2 \right\rangle & \sqrt{2}\left\langle S_{vh}{S_{hh}}^* \right\rangle \\ \left\langle S_{hh}{S_{vv}}^* \right\rangle & \sqrt{2}\left\langle S_{hh}{S_{vh}}^* \right\rangle & \left\langle |S_{hh}|^2 \right\rangle \end{bmatrix} \quad (1)$$

$$\rho_{co} = \left| \frac{\langle S_{vv}{S_{hh}}^* \rangle}{\sqrt{\left\langle |S_{vv}|^2 \right\rangle \left\langle |S_{hh}|^2 \right\rangle}} \right| \quad (2)$$

$$\mu = \frac{2\left[\mathrm{Re}\langle S_{vv}{S_{hh}}^* \rangle - \left\langle |S_{vh}|^2 \right\rangle \right]}{\left\langle |S_{vv}|^2 \right\rangle + 2\left\langle |S_{vh}|^2 \right\rangle + \left\langle |S_{hh}|^2 \right\rangle} \quad (3)$$

2.5. Physical Sample Collection

Physical samples were collected from distributed locations within the contaminated tub. The locations were identified by the numbering scheme shown in Figure 3. Four sampling events occurred during the study period. The tub surface had limited space for taking samples, so we chose to have one sampling event before the diesel injection and three afterward. Samples collected throughout the experiment (S1, S2, and S3) were collected during periods when the radar was at rest, and along the edge of the tub. At the end of the experiment, samples were taken from the center of the tub (Figure 3, S4). Ice surface temperature was measured using a probe (Traceable Digital Thermometer, Control Company, accuracy of ±0.05 °C), and Kimwipe™ was used to determine if the surface of the ice was wet or not. Surface ice scrapings were collected using a metal spatula and bulk ice samples were cut from the ice volume using a hand bone saw. The ice thickness was measured, and the samples were subsequently segmented into upper ice core and lower ice core for laboratory analysis. Water samples of 1 L for seawater salinity were also collected below the ice surface and at the bottom of the contaminated tub. Air temperature and humidity were collected from the onsite automated weather station every minute, but the data were averaged to a 30 min time scale to create a time-series profile. Wind speed was collected from the "Winnipeg INTL A" weather station at Winnipeg Richardson International Airport, Manitoba, Canada, and was collected on an hourly basis.

Samples were processed to determine salinity, brine volume, and diesel fuel volume in the Centre for Earth Observation Science (CEOS) Chemistry Lab. Liquid diesel was pipetted from the surface of frozen samples and measured to determine the volume of diesel that was present on the surface of the ice. Frozen samples were then melted at room temperature and any diesel that was within the ice floated to the surface of the water. Diesel was then removed from the water surface and the volume of the diesel and remaining water were measured. The separated water was measured with a Cond 3310 m equipped with a TetraCon 325 probe to determine the bulk practical salinity. The reference salinity was then calculated using Equation (1) from [40]. Salinities of the clean water samples

were measured with an Orion Star A212-Thermo Scientific conductivity meter, and the reference salinity was subsequently calculated. We used two conductivity meters to ensure that there was no cross-contamination between clean and contaminated samples. After salinity measurements, empirical formulas were used to calculate the brine volumes of the ice [41].

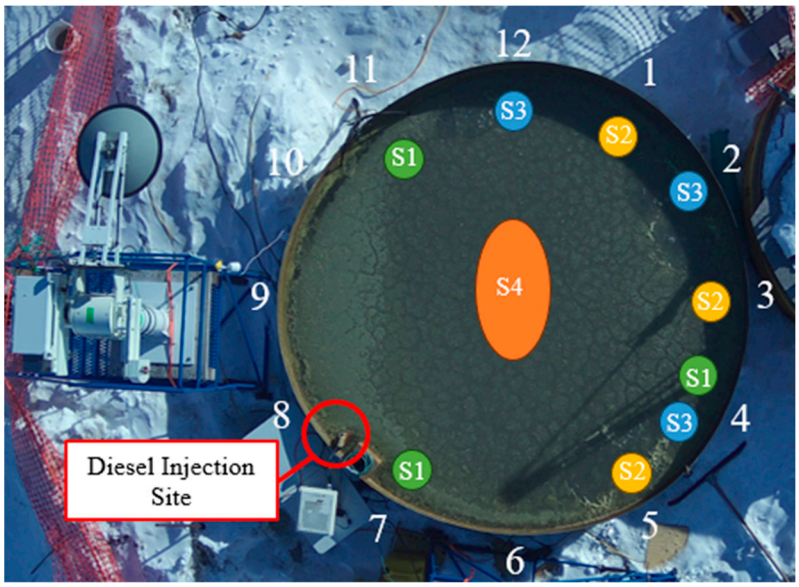


Figure 3. Physical Sampling Locations. S1: 7 March before oil injection, S2: 7 March after diesel injection, S3: 8 March, S4: 9 March.

3. Results

3.1. Experiment Overview

This study was initiated on March 6 at 08:30 CST when the heater was turned off in the experimental tub and ice was allowed to grow freely. Figure 4 shows the temporal evolution of the sea ice and experiment, as seen from the perspective of the CSCAT camera. At 21:30 on March 6, grease ice formed on the surface of the water, and by the next day (7 March), there was a thin layer of ice. The ice thickness was 4 cm at 11:00 on March 7. A total of 20 L of diesel fuel was injected underneath the ice on March 7 at 11:00. As the diesel was injected, it pooled underneath the ice and rose to the surface around the edge of the tub. The diesel then formed a narrow ring-shaped layer on the surface of the sea ice with the highest concentration remaining where the diesel was injected (Figure 4C). The diesel fuel on the surface became a slushy layer near the edges of the tub for the remainder of the study (Figure 4D,E). At the end of the experiment, after radar measurements were completed, we collected physical samples from the center of the tub (Figure 4F).

From the observed physical phenomenon, we defined three stages of development in this experiment. Stage 1 was defined as the time from the start of the experiment, when the tub had open water, and progressed until the beginning of sea ice formation (6 March, 2100). Stage 2 began with the initial formation of sea ice and ended once we saw the diesel visibly emerging onto the surface of the ice (March 8 07:30), we note that the diesel injection occurred during Stage 2. Stage 3 was identified with a backscatter drop and ended at the conclusion of the experiment. The separation of the stages will be described in the scatterometer data section of this paper.

Air temperature and relative humidity were both recorded on the meteorological station at SERF and the results for the study are presented in Figure 5. Air temperature (Figure 5) remained below 0 °C during the study, with the temperature reaching a minimum of −21.6 °C in the early hours of March 7 and a maximum of −3.5 °C in the afternoon on March 8. The air temperature remained above −15 °C for the remainder of the experiment. Relative humidity ranged from 46% to 83%, with relative humidity being lowest at the

beginning of the study, and highest towards the end (Figure 5). Wind Speed (Figure 5), was reported from the "Winnipeg INTL A" weather station at Winnipeg Richardson International Airport, Manitoba, Canada. Wind speeds stayed relatively consistent throughout the study period with both the maximum, 31 km/h, and minimum, 9 km/h, speeds occurring on the first day of the experiment.

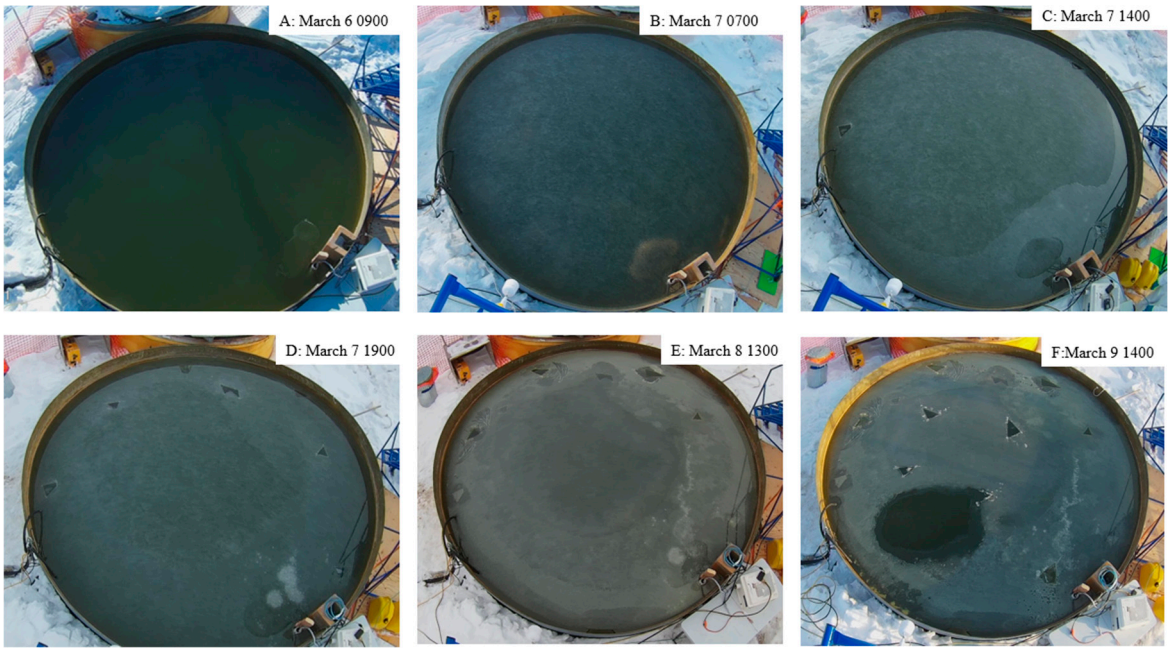


Figure 4. Temporal Progression of Ice Growth and Presence of Diesel Throughout the Study Period. (**A**) Start of Study, (**B**) Ice Formed, (**C**) After S1 and After Diesel Injection, (**D**) After S2, (**E**) After S3, (**F**) After S4 and End of Study.

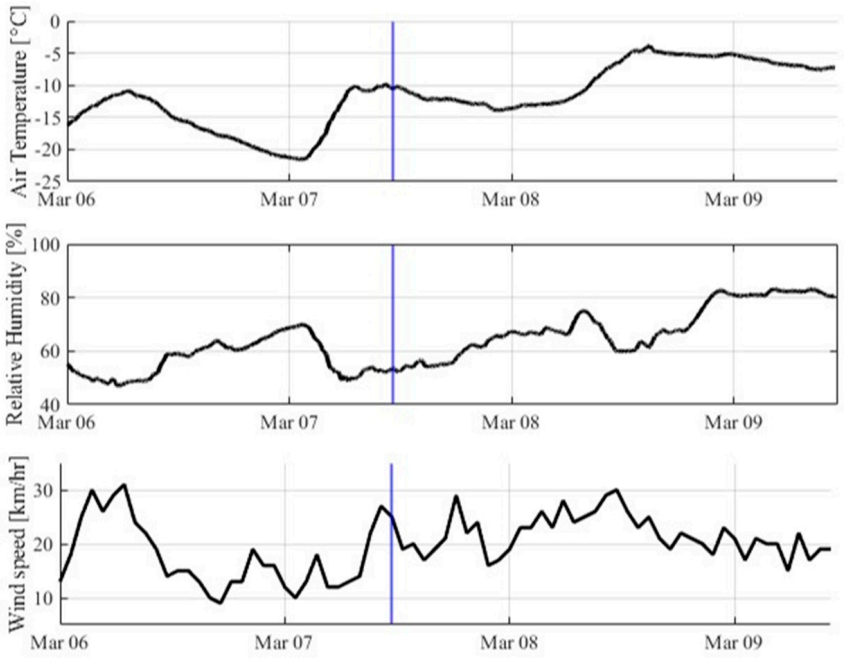


Figure 5. Temporal Variation of Air Temperature, Relative Humidity, and Wind Speed Throughout the Study Period. The Time of Diesel Injection is Marked by a Blue Line.

3.2. Scatterometer Results

NRCS values for C-band and the elevation incidence angles of 20° and 25° were plotted in a time series to establish the radar response throughout the study period. In Figure 6, σ_{VV} is the color black (abbreviated as VV), σ_{HH} is the color blue (abbreviated as HH), and σ_{HV} is the color red (i.e., cross-polarized signal, or HV). The results of the ρco and μ parameters for 20° and 25° are presented in Figure 7.

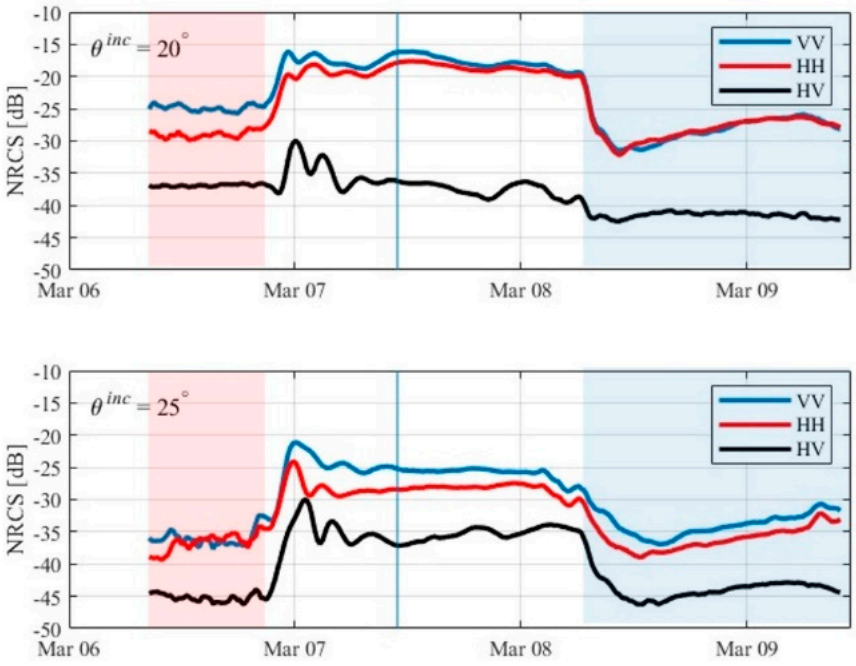


Figure 6. C-band NRCS Values for the study period at the 20° and 25° incidence angles. The red shaded area is Stage 1, the non-shaded area is Stage 2, and the blue shaded area is Stage 3. The blue line denotes the time of diesel injection.

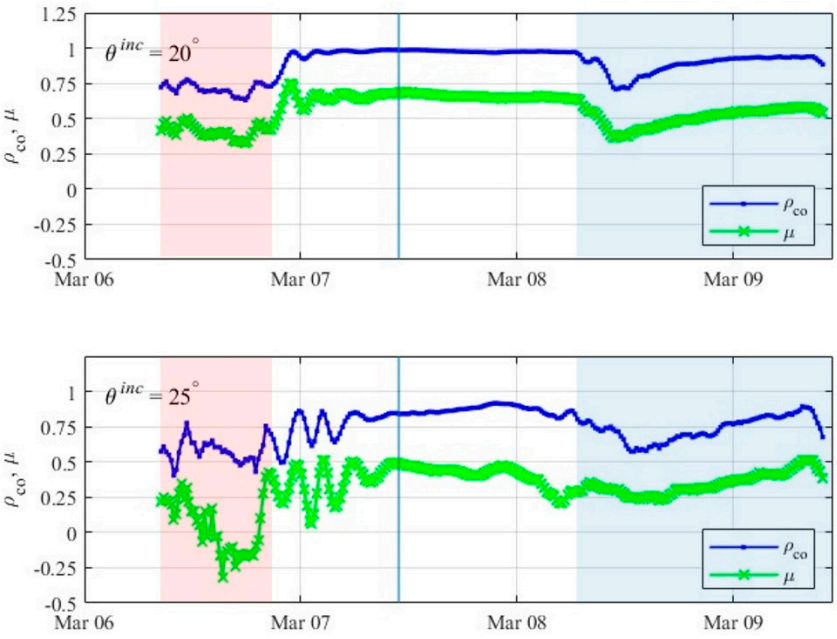


Figure 7. Copolarization correlation coefficient (ρco) and conformity coefficient (μ) for the 20° (upper panel) and 25° (lower panel) incidence angles. The red-shaded area is stage one, the non-shaded area is stage two, and the blue-shaded area is stage three. A solid vertical blue line denotes the time of diesel injection.

At the beginning of the experiment, the tub contained open water and the NRCS values were relatively stable (Figure 6). We defined this as "Stage 1." The 20° incidence angle was much flatter than the 25° and all of the polarizations are distinguishable. At 25°, the VV and HH polarizations are similar. The NRCS values were greater for all polarizations at the 20° incidence angle than the 25° incidence angle. The ρco and μ parameters were relatively constant at the 20° incidence angle (Figure 7). At a 25° incidence angle, ρco was also relatively constant. The μ-parameter showed a transient behavior starting from a positive value and transitioning to a negative value. Similarly to the NRCS, the values for ρco and μ at the 25° incidence angle were lower than the 20° angle, although there is more variability within the values.

The formation of a thin layer of grease ice at 21:30 March 6 resulted in significant changes in VV and HH NRCS values. We denoted this as the beginning of Stage 2. The greatest increase in NRCS was in the HV polarization with an observed change of 12.32 dB at an incidence angle of 25°. VV polarization also had a large increase of 12.18 dB (Table 2). For the 20° incidence angle, ρco and μ exhibited a transition (similar to the NRCS) and then reached a steady state with the presence of ice (Figure 7, upper panel). ρco and μ for the 25° incidence angle also exhibited a transient behavior as the ice began to form, before reaching a relatively stable value. Towards the end of Stage 2, both ρco and μ showed a slight decrease. Diesel fuel was injected at 11:00 on 7 March 2023, underneath a layer of sea ice which had a thickness of 3.6 cm. Small variations in the NRCS, ρco, and μ were observed throughout the period, but an immediate response to the diesel injection was not evident.

Table 2. Average change in Measured NRCS (dB) for the transition between phases of the experiment. The transition between Stages 1 and 2 accounts for the increase in backscatter at the start of Stage 2. The transition between Stage 2 and 3 accounts for the decrease in backscatter at the start of Stage 3.

	Transition from Stage 1 to Stage 2			**Transition from Stage 2 to Stage 3**		
Incidence Angle	**ΔVV [dB]**	**ΔHH [dB]**	**ΔHV [dB]**	**ΔVV [dB]**	**ΔHH [dB]**	**ΔHV [dB]**
20°	7.52	9.49	3.78	−11.85	−11.22	−2.90
25°	12.18	7.07	12.32	−7.10	−7.97	−11.09

Stage 3 started when there was an observed pronounced decline in NRCS for both incidence angles, midday March 8 (Figure 6), 18 h after the diesel injection. Simultaneously, we observed the diesel on the surface of the ice. The 20° incidence angle had a more notable change when compared to the 25° incidence angle as all polarizations had large decreases in radar return, and only HV had a large change at 25°. The greatest decreases occurred at the 20° incidence angle, 11.85 dB, occurred at the VV polarization and 11.22 dB, and occurred at HH (Table 2). After the initial decrease in NRCS for all polarizations and incidence angles, the values slowly increased for the remainder of the study. The copolarization and conformity coefficients for the 20° incidence angle followed a similar pattern to the NRCS, with a drop occurring at the start of Stage 3 and a slow increase in values for the remainder of the study (Figure 7). The ρco and μ values for 25° exhibited a similar trend to the measurement results at 20°.

3.3. Physical Results

Physical samples were collected in four sampling events throughout the study period, where S1 occurred during Stage 1 of the experiment, S2 during Stage 2, and S3 and S4 during Stage 3. For every sampling event, three sites were used (Figure 3), and the results are presented in Table 3. Sea ice thickness grew from 0 cm to 3.6 cm within 24 h of turning the heaters in the tub off. Following the injection of diesel at 1100 CST on March 7 the sea ice continued to grow until it reached an average thickness of 7cm on March 9. Sea ice salinity significantly decreased as the ice grew from S1 to S3, but there was an increase in

surface salinity between S3 and S4 sampling events. Seawater salinity remained relatively stable throughout the study, with concentration increasing from 21.6 g/kg to 22.1 g/kg by the end of the experiment. Diesel fuel was only detected for sea ice surface and sea ice core samples in the S3 sampling event. All other samples had negligible amounts.

Table 3. Physical Sampling Results.

	S1			**S2**			**S3**			**S4**		
Date	**7 March 0930 CST**			**7 March 1500 CST**			**8 March 1100 CST**			**9 March 1100 CST**		
Sampling Site	11	7	4	1	3	5	2	4	12	1	2	3
Sea ice thickness (cm)	3.6	3.6	3.6	4.5	4.3	3.6	6.6	6.1	6.6	7.5	7.0	6.5
Sea ice surface temperature (°C)	−3.9	−3.9	−3.9	−3.9	−3.9	−3.9	−3.4	−3.4	−3.4	−2.6	−2.6	−2.6
Sea ice core temperature (top) (°C)	−2.8	−2.6	−3.0	−2.5	−2.2	−2.5	−2.4	−3.4	−3.4	−1.5	−2.1	−1.9
Sea ice core temperature (bottom) (°C)	-	-	-	-	-	-	−1.56	−1.29	−1.74	−1.56	−1.29	−1.36
Sea ice surface scraping reference salinity (g/kg)	40.6	32.8	39.8	27.2	12.7	25.9	7.4	10.1	17.9	25.0	24.6	22.0
Sea ice core (top) bulk reference salinity (g/kg)	10.8	10.5	10.6	8.8	8.6	8.0	7.0	6.4	6.1	7.0	6.9	6.6
Sea ice core (bottom) bulk reference salinity (g/kg)							8.2	7.8	8.3	7.3	7.1	7.1
Seawater reference salinity (g/kg)	21.6	21.6	21.6	21.7	21.7	21.6	22.1	22.1	22.1	22.1	22.1	22.1
Brine ice core (top) Volume (mL)	66.0	65.8	95.6	59.6	68.3	35.4	70.0	57.6	54.6	67.3	46.3	38.2
Brine ice core (bottom) Volume (mL)	-	-	-	-	-	-	81.8	82.6	55.8	63.3	64.4	59.1
Sea ice surface diesel Volume (mL)	-	-	-	0	0	0	19.2	21.9	18.0	0	0	0
Sea ice core diesel (top) volume (mL)	-	-	-	0	0	0	13.00	0.9	5.0	0	0	0
Sea ice core diesel (bottom) volume (mL)	-	-	-	0	0	0	0	0	0	0	0	0
Seawater diesel volume (mL)	-	-	-	0	0	0	0	0	0	0	0	0

During physical sampling, before cutting the surface or extracting physical samples, we used a Kimwipe™ to assess the wetness of the surface. For S1, the surface was dry and for S2, we observed a trace amount of surface wetness. In Stage 3, we observed surface wetness during S3 and S4 sampling events.

4. Discussion

This paper presented an investigation into the response of a surface-based multipolarized C-band scatterometer to the introduction of diesel fuel underneath newly formed sea ice. The results of the study were used to gain insight into the usability of C-band for the monitoring of a freeze-up event, determining how C-band responds to changes in the thermodynamic properties of sea ice and how well the C-band frequency can detect the introduction of diesel fuel. We measured the temporal evolution of C-band scattering signatures throughout the experiment, accompanied by four physical sampling events and monitoring of meteorological conditions. This study aimed to build on the knowledge of how a multipolarized C-band scatterometer system responds to the introduction of diesel fuel to a young sea ice environment. Specific objectives were accomplished by (1) measuring and evaluating the time-series C-band scattering signatures during a freeze-up event, (2) assessing how C-band responds to changes in the thermodynamic properties of newly formed sea ice, and (3) analyzing how the polarimetric C-band results can be used to detect changes in response to the introduction of diesel fuel.

4.1. Meteorological Conditions and Physical Measurements

We began the experiment from an open water configuration, which we considered a baseline for the experiment. Wind speeds were highly variable throughout Stage 1 but remained below the threshold to classify it as 'windy'. At the beginning of Stage 2, air

temperature reached the study minimum of −21.6 °C overnight on 7 March with the second lowest recorded wind speed of 10 km/h, which promoted the transition from grease ice to a thin layer of ice by the early morning of 7 March. During Stage 3 of the experiment, air temperature reached a maximum of −3.5 °C, relative humidity was highest with a maximum of 83% and the wind remained stable with limited variation in speeds. Between S2 and S3, sea ice continued to grow and reached a thickness ranging from 6.1 cm to 6.6 cm which is likely not impacted by the negligible and small amounts of diesel fuel that were present in each sampling event. A study conducted by [9] noted that only large amounts of oil (on the ice surface) reduced sea ice growth. For instance, [9] noted that a crude oil fraction of ~8% reduced sea growth by ~36%. Compared to [9], our experiment only reached a max diesel fuel fraction of ~2.7% in the ice. Moreover, near-transparent diesel fuel does not reduce sea ice albedo in the same manner as black crude oil and, therefore, does not considerably warm the ice. However, surfaced diesel fuel can act to prevent heat from escaping the ice since diesel has a lower thermal conductivity (~0.12 $W \cdot m^{-1} \cdot K^{-1}$) [42] than sea ice (~2 $W \cdot m^{-1} \cdot K^{-1}$) [43] and seawater (~0.56 $W \cdot m^{-1} \cdot K^{-1}$) [44]. The relatively low volumes of surfaced diesel may have limited its effect on ice temperature. Notably, sea ice temperature increased to −3.35 °C which is expected as there was an increase in air temperature. Sea ice surface scraping reference salinity ranged from 7.43 g/kg to 17.88 g/kg and sea ice core salinity ranged from 6.12 g/kg to 7.03 g/kg in the top half and 7.83 g/kg to 8.33 g/kg in the bottom half. The decreases in salinity when compared to S2 and variation in the salinity for the top ice cores versus the bottom ice cores are likely due (in part) to the warm air and sea ice temperatures. Sea ice salinity and brine volume both decreased throughout the experiment, which is expected as ice ages and the salinity and brine volume content decrease due to being expelled out of the ice column through fluid movement enabled by warm sea ice and air temperatures [45,46]. The S3 samples had recorded volumes of diesel fuel present on the surface and within the sea ice. Volumes ranged from 18.0 mL to 21.9 mL on the surface of the ice and 0.9 mL to 13.0 mL within the ice cores. Ice temperatures greater than −5 °C are known to be permeable to fluid movement, including the vertical migration of diesel through the sea ice [9,30,46]. This is why we observed a vertical movement of diesel fuel to the surface of the ice, possibly contributing to the subsequent decrease in sea ice salinity as the brine may have been displaced downward towards the ice bottom and water column.

For the sampling locations chosen for S4, diesel was not noted on the ice surface or within the ice, although while sampling, observations were made that diesel was present on the surface of the water. This is likely a result of the oil pooling in locations rather than uniformly spreading out underneath the sea ice, which is a result of the small volume of diesel introduced to the experiment. In small, simulated oil spills, there have been observations made that indicate a greater vertical than horizontal movement of oil in a sea ice environment, which can be attributed to why diesel was not present throughout all of the ice samples [8,9]. The sampling sites for S4 were collected in the center of the tub, which explains why there was no diesel present in the ice core samples, as the diesel fuel pooled around the edges of the tub and was concentrated near the injection site (Figure 3). Additionally, the lack of diesel fuel present in the S4 sampling sites could also be a result of evaporative loss of diesel from the surface of the ice, as the S3 sampling event only had 0.9 mL–13.0 mL of diesel within the ice surface. The warm air temperatures and sunny conditions that occurred before S4 likely promoted the evaporation of any diesel that was on the ice surface owing to the high concentrations of volatile components found in diesel fuel [24].

4.2. Scatterometer Measurements

In this study, we investigated the C-band scattering response of a diesel spill injected beneath a thin sea ice layer through a time-series measurement campaign. Based on our initial assessment and evaluation of the physical and scattering properties of the

experimental sea ice surface, we identified three distinctive stages: Stage 1—open water; Stage 2—thin sea ice; and Stage 3—diesel on sea ice.

4.2.1. Stage 1: Open Water

Microwave radar systems are capable of observing freeze-up events but there is a need for a greater understanding of the scattering mechanisms and radar response when monitoring these situations [11,21]. Overall, the results of the NRCS for Stage 1 of this experiment are consistent with the field-based findings of [11] and oil-tub based results of [25] where open water conditions in an experimental tub result in variable but somewhat consistent backscatter return. Another study by [47] found that C-band VV NRCS at 21° ranged from −9 dB to −25 dB with variations in the wind. It was also found that with increasing incidence angle the impact of the wind increases. Our NRCS values were around −25 dB for VV, −30 dB for HH, and −37 dB for HV at the 20° incidence angle and −35 dB for VV, −37 dB for HH, and −45 dB for HV at the 25° incidence angle (Figure 6). These values are lower than what was observed by [47] but this is a result of the difference in wind speeds throughout the study. Low values NRCS values for all polarizations at C-band are expected for a smooth water surface, both theoretically and experimentally.

The ρco and μ parameters results for Stage 1 at 20° and 25° incidence angles are presented in Figure 7. The co-polarization correlation coefficient, ρco, is a measure of similarity between VV and HH channels and it ranges from 0 to 1. Small values suggest a decorrelation process (such as multiple scattering from brine pockets or scattering from the ice/water interface as the sea ice forms) and typically ρco decreases with increasing incidence angle for young sea ice scattering measurements. The conformity coefficient, μ, is sensitive to surface roughness, and provides a distinction between co-polarized and cross-polarized responses. Generally, smooth surfaces have negative values and rough surfaces have positive values. During the ice formation, ρco fluctuated by about 0.7 for both incidence angles. These observed values are greater than those reported by [17], who found clusters of values around 0.2 for the open-water stage. In the case of the μ-parameter at 20° incidence angle, the values were clustered around 0.5. However, the study indicated the values for μ around −0.2 and gradually declined to −0.6 before solid ice was seen. For the 25° angle, μ values also exceeded those previously recorded, although they showed a comparable trend to the result reported by [17], which used a 24.5° angle. The observed decline in the μ-parameter during Stage 1 might relate to the specific incidence angles used or to the onset of ice formation. This contrasts with the findings of [39], where no decrease in μ-parameter was observed in open water, but consistently low values were reported.

4.2.2. Stage 2: Thin Sea Ice

Stage 2 began with the initial formation of sea ice from open water. After the sea ice was formed and consistent across the tub, we injected diesel beneath the ice and continued to monitor the surface using the scatterometer. Stage 2 ended when we observed diesel emerging on the surface, which coincided with the rapid decrease in NRCS.

As seen in Figure 6, the radar returns of all three polarizations assessed in this study increased throughout Stage 2 of the experiment until a solid ice sheet formed. The largest change between Stage 1 and Stage 2 was observed to be 11.48 dB for the VV polarization and the incidence angle of 25°. Although HV also had a significant change of 10.13 dB. The increase in backscatter during the transition from Stage 1 to Stage 2 could be used to determine and monitor freeze-up events in the Arctic. The NRCS values remained consistent throughout Stage 2 with NRCS values centered around −16 dB for VV, −18 dB for HH, and −37 dB for HV at the 20° incidence angle, while the 25° incidence angle had values around −25 dB for VV, −28 dB for HH and −35 dB for HV. These values are similar to those found by [11] in a young sea ice environment, where VV was around −15 dB, HH was around −18 dB, and HV was around −36 dB at the 30° incidence angle. Reference [31] also found that in an experimental tub with thin sea ice, the NRCS for VV was around −16 dB, and HH was around −19 dB for the 60° incidence angle. As previously noted,

the diesel was injected during Stage 2 at 11:00 on March 7 and there was no immediate response in the NRCS. Both [25] and [45] noted that there was a delay in the response of the radar backscatter to the introduction of oil products which has been attributed to the time it took for the oil to migrate upwards through the ice to the surface [24]. There was an immediate decrease in the measured NRCS values for the study conducted by [48], but the ice was thinner than the two previous studies which could have resulted in the oil being detected underneath the sea ice.

During Stage 2, the ρco and μ parameters for 20° showed an initial transient behavior and then reached a relatively stable value once the sea ice was formed. The 25° incidence angle for ρco and μ values exhibited an even greater oscillation throughout the initial increase when the ice was formed but remained relatively stable during the remainder of stage two around 0.8 (ρco) and 0.15 (μ). Previous studies have shown that there is a significant relationship between sea ice thickness and the ρco-parameter, where thicknesses less than 6cm show greater variability than those greater than 8 cm [11,17]. Ice thickness during stage 2 was less than 6cm, but due to the rate of ice growth, we would expect it to be near the value of 1, which was observed in this study. The ρco values observed in this study were around 1 for the 20° incidence angle and 0.8 for the 25° incidence angle. These results are similar to what was found by [11] who both noted ρco values for bare, young sea ice to be 0.9 at the 25° and 20° incidence angles respectively. Reference [17] reported ρco values around 0.8 for the 24.5° incidence angle, while a study conducted by [49] reported a value of 0.5 for ρco at 25°. Similarly to the NRCS for Stage 2, there was no response in the ρco and μ parameters when the diesel was introduced.

4.2.3. Stage 3: Emergence of Diesel on Sea Ice

There is limited knowledge on the usability of C-band for the detection of diesel fuel and this study addresses this knowledge gap in a prevalently used oil product. The diesel was observed on the sea ice surface approximately 18 h after its introduction. In this study, decreases of 11.85 dB (VV), 11.22 dB (HH), and 2.90 dB (HV) were measured for the 20° incidence angle for stage three, while decreases of 7.10 dB (VV), 7.97 dB (HH), and 11.09 dB (HV) were noted for the 25° incidence angle (Table 2). The cross-polarization value for the 20° incidence angle experienced a minimal decrease in NRCS, which is likely because the cross-polarized signal is already near the noise floor of the instrument and the backscattering power levels are extremely low. Decreases in cross-polarized NRCS were also observed by [25], but there were noted increases in VV and HH NRCS when oil migrated to the ice surface. Reduction in all polarimetric parameters when oil is present was also observed by [48] who noted decreases of approximately 6 dB for VV, 9 dB for HH, and 5 dB for VH.

The decrease in NRCS values observed on 8 March (Figure 6) coincides with an increase in air temperature (Figure 5), a decrease in sea ice surface salinity, and observation of diesel at the surface of the ice (Table 3). Additionally, March 8 was the first day there was a large decrease in sea ice surface scraping salinity, and a marginal decrease in the sea ice core salinity (Table 3); both of which support the observed decrease in NRCS (Figure 6) as a result of these changes in physical properties resulting from an increase in air temperature. In warm conditions that promote fluid movement through sea ice, diesel fuel was likely to migrate vertically through brine channels in the sea ice as has been previously observed with corn and crude oil [24,30]. The increase in brine volume (Table 3) with the warm air temperature likely resulted in both brine drainage and a vertical movement of diesel fuel through brine channels, as there were measurable amounts of diesel volume in the ice cores and on the surface of the sea ice. The vertical movement and presence of diesel in and on the sea ice would contribute to a decrease in the NRCS values. There is a dielectric loss with the reduction in sea ice salinity resulting from the presence of diesel fuel as well as increased liquid on the surface, creating a smoother surface. Physical properties of sea ice and their changes resulting from fluctuations in air temperature and the presence of diesel fuel contribute to changes in C-band scatterometer NRCS.

The ρco and μ parameters analyses for the diesel injection at the 20°and 25° incidence angles are presented in Figure 7. During Stage 3, a sharp decline in both coefficients was observed. Following the decrease the μ and ρco values continued to slowly rise for the remainder of the experiment to values of 0.55 and 0.95, respectively, resulting in a local minimum in the time-series. The μ and ρco values for the 25° incidence angle followed a different pattern than the 20° angle, as both values fluctuated throughout the whole time that ice was present in the experimental tub. The results of the ρco analysis were more stable but ranged from 0.8–0.9 before a drop occurred similar to that was observed for the 20° incidence angle. Although a similar drop occurred for ρco, there was a higher degree of variation in the values at the 25° incidence angle than at 20°. The μ-parameter fluctuated to a higher degree than ρco as values ranged from 0.3–0.5, before a small decrease occurred at the same time the drops were observed for the other coefficients and incidence angles. Unlike the other drops that occurred there was a second spike and decrease in μ before the values slowly rose towards the end of the study. Similar trends in μ and ρco were observed by [17], this is likely a result of similar incidence angles being used as well as the finding that the ρco values are susceptible to surface scattering at incidence angles less than 30° [49]. The scattering methods can be determined through the similarity of the coefficient trends to the NRCS values. In both this study and the study conducted by [17] and [49], the ρco-parameter followed trends more similar to the NRCS trends when compared to the μ-parameter.

5. Conclusions

The goal of this study is to build on the understanding of how a multipolarized C-band scatterometer system responds to the introduction of diesel fuel underneath newly formed sea ice. This was achieved by (1) measuring and evaluating the time-series C-band scattering signatures during a freeze-up event, (2) assessing the C-band response to thermodynamic property changes in newly formed sea ice, and (3) analyzing how the polarimetric C-band results can be used to detect changes.

We characterized the microwave C-band scattering response of sea ice growing from seawater in a mesocosm tub. There were significant increases in the received backscatter during the transition from stage one (open water) to stage two (newly-formed sea ice) in the VV polarization for both 20° and 25° incidence angles and notable changes for HH and HV at both incidence angles. These results can be used to develop standardized methods to monitor freeze-up events in the Arctic using satellite data (e.g., RADARSAT-2). Our findings provide detailed time-series data in a rapidly changing environment, as the transition from open water to newly formed sea ice occurred over several hours.

There was no large change in NRCS for 20° and 25° incidence angles immediately following the introduction of diesel fuel underneath the sea ice in stage two. We observed diesel emerging onto the sea ice surface approximately 18 h after its introduction shortly after there was a decrease in NRCS. During stage three there was a large decrease in the NRCS values for 20° and 25°, along with a migration of diesel fuel to the surface and a decrease in ice core salinity. The observed decrease in NRCS is due to the change in salinity of the sea ice and the presence of diesel fuel on the surface of the ice, furthering the conclusion that C-band is sensitive to changes in thermodynamic properties and can be used to detect the presence of oil products in the Arctic Sea ice environment. It is recommended that the 20° incidence angle and both VV and HH polarizations be used to monitor the presence of diesel fuel in a young sea ice environment. Furthermore, both VV and HH had large observed decreases in backscatter when the diesel migrated to the surface of the ice and the salinity decreased, owing to the combination of brine drainage and brine displacement from upward diesel migration. This was likely enhanced by warming ambient conditions.

We note that the elevation angles in this study can be acquired using RCM and Radarsat-2 standard or ScanSAR modes. Consequently, a connection between our experimental data and satellite data can be obtained. High temporal resolution measurements are

the benefit of the near-surface scatterometer data, while satellite imagery has an advantage in the broad spatial scale. Therefore, the results of these near-surface experiments may assist in drawing connections between the satellite images, which might be several days apart. From an operational perspective, these connections still need further research to achieve their potential. We suggest that the results of our studies could be used to critically investigate and monitor regions of interest, such as active ports and/or transportation corridors near communities.

It is recommended that future work be conducted in a larger experimental area with thicker sea ice so that multiple incidence angles can be used. This would allow for an easier interpretation of satellite data using these results, as well as build on the understanding of how diesel fuel can be detected in the sea ice environment. This study contributes to a greater understanding of how C-band frequencies can be used to monitor oil products in the Arctic and act as a baseline for the interpretation of satellite data. As well, these findings will assist in the development of standards for oil and diesel fuel detection in the Canadian Arctic in association with the Canadian Standards Association Group.

Author Contributions: Conceptualization, D.I.; Methodology, L.H., M.Z.M., D.S.D., K.P., G.A.S. and D.I.; Software, L.H., M.Z.M., E.A. and D.I.; Validation, L.H., M.Z.M., E.A., D.S.D., G.A.S. and D.I.; Formal analysis, L.H., M.Z.M., E.A. and D.I.; Investigation, L.H., M.Z.M., E.A. and D.I.; Resources, D.I.; Data curation, L.H. and D.I.; Writing—original draft, L.H.; Writing—review & editing, L.H., M.Z.M., E.A., D.S.D., K.P., G.A.S. and D.I.; Visualization, L.H., M.Z.M. and D.I.; Supervision, G.A.S. and D.I.; Project administration, G.A.S. and D.I.; Funding acquisition, G.A.S. and D.I. All authors have read and agreed to the published version of the manuscript.

Funding: This research was funded by Natural Sciences and Engineering Research Council, grant number: RGPIN-004974-2017; and Genome Canada, grant number: LSP20-18304.

Data Availability Statement: The data presented in this study are available on request from the corresponding author. As data were collected as part of the GENICE II project, access to the data will be facilitated through the project website: www.genice2.com.

Acknowledgments: The authors would like to express their gratitude to David Binne (SERF Technician, CEOS), Shiva Lashkari (Lab Technician, CEOS), and Lisa Oswald (Trace Contaminants Technician, CEOS) for their support.

Conflicts of Interest: The authors declare no conflicts of interest.

References

1. Comiso, J.C. Large Decadal Decline of the Arctic Multiyear Ice Cover. *J. Climatol.* **2012**, *25*, 1176–1193. [CrossRef]
2. Kwok, R. Arctic sea ice thickness, volume, and multiyear ice coverage: Losses and coupled variability (1958–2018). *Environ. Res. Lett.* **2018**, *13*, 105005. [CrossRef]
3. Dawson, J.; Pizzolato, L.; Howell, S.E.; Copland, L.; Johnston, M.E. Temporal and spatial patterns of ship traffic in the Canadian Arctic from 1990 to 2015. *Arctic* **2018**, *71*, 15–26. [CrossRef]
4. Gautier, D.L.; Bird, K.J.; Charpentier, R.R.; Grantz, A.; Houseknecht, D.W.; Klett, T.R.; Moore, T.E.; Pitman, J.K.; Schenk, C.J.; Schuenemeyer, J.H.; et al. Assessment of undiscovered oil and gas in the Arctic. *Science* **2009**, *324*, 1175–1179. [CrossRef] [PubMed]
5. Melia, N.; Haines, K.; Hawkins, E. Sea ice decline and 21st century trans-Arctic shipping routes. *Geophys. Res. Lett.* **2016**, *43*, 9720–9728. [CrossRef]
6. Arctic Council. AGREEMENT on Cooperation on Marine Oil Pollution Preparedness and Response in the Arctic. In Proceedings of the SAO Meeting, Whitehorse, NC, Canada, 22–23 October 2013.
7. National Research Council; Transportation Research Board; Marine Board; Division on Earth and Life Studies; Polar Research Board; Ocean Studies Board; Committee on Responding to Oil Spills in the U.S. *Arctic Marine Environment. Arctic Marine Environment*; National Academies Press: Washington, DC, USA, 2014.
8. Wilkinson, J.; Beegle-Krause, C.J.; Evers, K.U.; Hughes, N.; Lewis, A.; Reed, M.; Wadhams, P. Oil spill response capabilities and technologies for ice-covered Arctic marine waters: A review of recent developments and established practices. *Ambio* **2017**, *46*, 423–441. [CrossRef] [PubMed]
9. Desmond, D.S.; Saltymakova, D.; Neusitzer, T.D.; Firoozy, N.; Isleifson, D.; Barber, D.G.; Stern, G.A. Oil Behavior in Sea Ice: Changes in Chemical Composition and Resultant Effect on Sea Ice Dielectrics. *Mar. Pollut. Bull.* **2019**, *142*, 216–233. [CrossRef] [PubMed]

10. Rivas, M.B.; Otosaka, I.; Stoffelen, A.; Verhoef, A. A Scatterometer Record of Sea Ice Extents and Backscatter: 1992–2016. *Cryosphere* **2018**, *12*, 2941–2953. [CrossRef]
11. Isleifson, D.; Hwang, B.; Barber, D.G.; Scharien, R.K.; Shafai, L. C-Band Polarimetric Backscattering Signatures of Newly Formed Sea Ice During Fall Freeze-Up. *IEEE Trans. Geosci. Remote Sens.* **2010**, *48*, 3256–3267. [CrossRef]
12. Nandan, V.; Geldsetzer, T.; Islam, T.; Yackel, J.J.; Gill, J.P.S.; Fuller, M.C.; Gunn, G.; Duguay, C. Ku-, X-and C-band measured and modeled microwave backscatter from a highly saline snow cover on first-year sea ice. *Remote Sens. Environ.* **2016**, *187*, 62–75. [CrossRef]
13. Ouchi, K. Recent trend and advance of synthetic aperture radar with selected topics. *Remote Sens.* **2013**, *5*, 716–807. [CrossRef]
14. Cloude, S.R.; Pottier, E. A Review of Target Decomposition in Radar Polarimetry. *IEEE Trans. Geosci. Remote Sens.* **1996**, *34*, 498–518. [CrossRef]
15. Shokr, M.E.; Wilson, L.J.; Surdu-Miller, D.L. Effect of Radar Parameters on Sea Ice Tonal and Textural Signatures Using Multi-Frequency Polarimetric SAR Data. *Photogramm. Eng. Remote Sens.* **1995**, *6*, 1463–1473.
16. Gill, J.P.S.; Yackel, J.J. Evaluation of C-band SAR polarimetric parameters for discrimination of first-year sea ice types. *Can. J. Remote Sens.* **2012**, *38*, 306–323. [CrossRef]
17. Asihene, E.; Stern, G.; Barber, D.G.; Gilmore, C.; Isleifson, D. Toward the Discrimination of Oil Spills in Newly Formed Sea Ice Using C-Band Radar Polarimetric Parameters. *IEEE Trans. Geosci. Remote Sens.* **2023**, *61*, 4300115. [CrossRef]
18. Shokr, M.; Nirmal, S.K. *Sea Ice: Physics and Remote Sensing*; John Wiley & Sons: Hoboken, NJ, USA, 2015.
19. Onstott, R.G. SAR and scatterometer signatures of sea ice. In *Microwave Remote Sensing of Sea Ice*; Carsey, F.D., Ed.; American Geophysical Union: Washington, DC, USA, 1992; pp. 73–104.
20. Hallikainen, M.; Winebrenner, D. The physical basis for sea ice remote sensing. In *Microwave Remove Sensing of Sea Ice*; Carsey, F.D., Ed.; American Geoph: Washington, DC, USA, 1992; pp. 29–46.
21. Drinkwater, M.R.; Kwok, R.; Rignot, E.; Israelsson, H.; Onstott, R.G.; Winebrenner, D.P. *Microwave Remote Sensing of Sea Ice*; Carsey, F.D., Ed.; American Geophysical Union: Washington, DC, USA, 1992; Volume 68.
22. Zhang, B.; Perrie, W.; Li, X.; Pichel, W.G. Mapping sea surface oil slicks using RADARSAT-2 quad-polarization SAR image. *Geophys. Res. Lett.* **2011**, *38*, L10602. [CrossRef]
23. Wadhams, P. *Ice in the Ocean*; CRC Press: Boca Raton, FL, USA, 2014.
24. Desmond, D.S.; Neusitzer, T.D.; Firoozy, N.; Isleifson, D.; Lemes, M.; Barber, D.G.; Stern, G.A. Examining the physical processes of corn oil (medium crude oil surrogate) in sea ice and its resultant effect on complex permittivity and normalized radar cross-section. *Mar. Pollut. Bull.* **2019**, *142*, 484–493. [CrossRef]
25. Asihene, E.; Desmond, D.S.; Harasyn, M.L.; Landry, D.; Veenaas, C.; Mansoori, A.; Fuller, M.C.; Stern, G.; Barber, D.G.; Gilmore, C.; et al. Toward the Detection of Oil Spills in Newly Formed Sea Ice Using C-Band Multipolarization Radar. *IEEE Trans. Geosci. Remote Sens.* **2021**, *60*, 4302615. [CrossRef]
26. Huffines, E. *Arctic Standards Recommendations on Oil Spill Prevention, Response, and Safety in the U.S. Arctic Ocean*; Pew Charitable Trusts: Philadelphia, PA, USA, 2013.
27. Kuppusamy, S.; Maddela, N.R.; Megharaj, M.; Venkateswarlu, K. *Total Petroleum Hydrocarbons. Environmental Fate, Toxicity, and Remediation*; Springer: Cham, Switzerland, 2020.
28. Oggier, M.; Eicken, H.; Wilkinson, J.; Petrich, C.; O'Sadnick, M. Crude oil migration in sea-ice: Laboratory studies of constraints on oil mobilization and seasonal evolution. *Cold Reg. Sci. Technol.* **2020**, *174*, 102924. [CrossRef]
29. Martin, S. A field study of brine drainage and oil entrainment in first year sea ice. *J. Glaciol.* **1979**, *22*, 473–502. [CrossRef]
30. Saltymakova, D.; Desmond, D.S.; Isleifson, D.; Firoozy, N.; Neusitzer, T.D.; Xu, Z.; Lemes, M.; Barber, D.G.; Stern, G.A. Effect of dissolution, evaporation, and photooxidation on crude oil chemical composition, dielectric properties and its radar signature in the Arctic environment. *Mar. Pollut. Bull.* **2020**, *151*, 110629. [CrossRef] [PubMed]
31. Firoozy, N.; Neusitzer, T.; Desmond, D.; Tiede, T.; Lemes, M.; Landy, J.; Mojabi, P.; Rysgaard, S.; Stern, G.; Barber, D. An electromagnetic detection case study on crude oil injection in a young sea ice environment. *IEEE Trans. Geosci. Remote Sens.* **2017**, *55*, 4465–4475. [CrossRef]
32. Isleifson, D.; Harasyn, M.L.; Landry, D.; Babb, D.; Asihene, E. Observations of Thin First Year Sea Ice Using a Suite of Surface Radar, LiDAR, and Drone Sensors. *Can. J. Remote Sens.* **2023**, *49*, 2226220. [CrossRef]
33. Brekke, C.; Holt, B.; Jones, C.; Skrunes, S. Discrimination of Oil Spills from Newly Formed Sea Ice by Synthetic Aperture Radar. *Remote Sens. Environ.* **2014**, *145*, 1–14. [CrossRef]
34. Brekke, C.; Solberg, A.H. Oil spill detection by satellite remote sensing. *Remote Sens. Environ.* **2005**, *95*, 1–13. [CrossRef]
35. Johansson, A.M.; Brekke, C.; Spreen, G. Multi-frequency polarimetric SAR signatures of lead sea ice and oil spills. In Proceedings of the 2017 IEEE International Geoscience and Remote Sensing Symposium (IGARSS), Fort Worth, TX, USA, 23–28 July 2017; pp. 1872–1875.
36. Johansson, A.M.; Espeseth, M.M.; Brekke, C.; Holt, B. Can mineral oil slicks be distinguished from newly formed sea ice using synthetic aperture radar? *IEEE J. Sel. Top. Appl. Earth Observ. Remote Sens.* **2020**, *13*, 4996–5010. [CrossRef]
37. Prinsenberg, S.J. Salinity and temperature distributions of Hudson Bay and James Bay. In *Canadian Inland Seas*; Martini, I.P., Ed.; Elsevier Oceanography Series: Guelph, ON, Canada, 1986; Volume 44, pp. 163–186.

38. Isleifson, D.; Mead, J.B.; Fuller, M.C.; Hicks, L.; Desmond, D.; Asihene, E.; Stern, G.A.; Barber, D.G. A Multi frequency Suite of Polarimetric Scatterometers for Arctic Remote Sensing. In Proceedings of the URSI International Symposium on Electromagnetic Theory, Vancouver, BC, Canada, 22–26 May 2023.
39. Mayvan, M.Z.; Asihene, E.; Desmond, D.; Hicks, L.; Polcwiartek, K.; Stern, G.A.; Isleifson, D. Monitoring Diesel Spills in Freezing Seawater under Windy Conditions Using C-Band Polarimetric Radar. *Remote Sens.* **2024**, *16*, 379. [CrossRef]
40. Grekov, A.N.; Grekov, N.A.; Sychov, E.N. Estimating quality of indirect measurements of sea water sound velocity by CTD data. *Measurement* **2021**, *175*, 109073. [CrossRef]
41. Cox, G.F.N.; Weeks, W.F. Equations for determining the gas and brine volumes in sea-ice samples. *J. Glaciol.* **1983**, *29*, 306–316. [CrossRef]
42. Elam, S.K.; Tokura, I.; Saito, K.; Altenkirch, R.A. Thermal Conductivity of Crude Oils. *Exp. Therm. Fluid Sci.* **1989**, *2*, 1–6. [CrossRef]
43. Pringle, D.J.; Trodahl, H.J.; Haskell, T.G. Direct measurement of sea ice thermal conductivity: No surface reduction. *J. Geophys. Res. Oceans* **2006**, *111*. [CrossRef]
44. Sharqawy, M.H. New correlations for seawater and pure water thermal conductivity at different temperatures and salinities. *Desalination* **2013**, *313*, 97–104. [CrossRef]
45. Neusitzer, T.D.; Firoozy, N.; Tiede, T.M.; Desmond, D.S.; Lemes, M.J.; Stern, G.A.; Rysgaard, S.; Mojabi, P.; Barber, D.G. Examining the impact of a crude oil spill on the permittivity profile and normalized radar cross section of young sea ice. *IEEE Trans. Geosci. Remote Sens.* **2018**, *56*, 921–936. [CrossRef]
46. Golden, K.M. Brine percolation and the transport properties of sea ice. *Ann. Glaciol.* **2001**, *33*, 28–36. [CrossRef]
47. Carswell, J.R.; Donnelly, W.J.; McIntosh, R.E.; Donelan, M.A.; Vandemark, D.C. Analysis of C and Ku-band Ocean Backscatter Measurements under Low-Wind Conditions. *J. Geophys. Res. Oceans* **1999**, *104*, 20687–20701. [CrossRef]
48. Firoozy, N.; Neusitzer, T.; Chirkova, D.; Desmond, D.S.; Lemes, M.J.; Landy, J.; Mojabi, P.; Rysgaard, S.; Stern, G.; Barber, D.G. A controlled experiment on oil release beneath thin sea ice and its electromagnetic detection. *IEEE Trans. Geosci. Remote Sens.* **2018**, *56*, 4406–4419. [CrossRef]
49. Nghiem, S.V.; Kwok, R.; Yueh, S.H.; Drinkwater, M.R. Polarimetric signatures of sea ice 2. Experimental Observations. *J. Geophys. Res.* **1995**, *100*, 13681–13698. [CrossRef]

Disclaimer/Publisher's Note: The statements, opinions and data contained in all publications are solely those of the individual author(s) and contributor(s) and not of MDPI and/or the editor(s). MDPI and/or the editor(s) disclaim responsibility for any injury to people or property resulting from any ideas, methods, instructions or products referred to in the content.